High cycle fatigue behavior and life prediction for additively manufactured 17-4 PH stainless steel: Effect of sub-surface porosity and surface roughness

Simone Romano[a], P.D. Nezhadfar[b,c], Nima Shamsaei[b,c], Mohsen Seifi[d,e], Stefano Beretta[a,*]

[a] Department of Mechanical Engineering, Politecnico di Milano, Via La Masa 1, 20156 Milan, Italy
[b] Department of Mechanical Engineering, Auburn University, Auburn, AL 36849, USA
[c] National Center for Additive Manufacturing Excellence (NCAME), Auburn University, Auburn, AL 36849, USA
[d] Department of Materials Science and Engineering, Case Western Reserve University, Cleveland, OH 44106, USA
[e] ASTM International, Washington, DC, 20036, USA

ARTICLE INFO

ABSTRACT

The high potential of additive manufacturing (AM) techniques offers novel opportunities and unexplored design freedom. However, typical internal defects and poor surface quality inherent to AM process not only cause a lower fatigue resistance, but also more scatter in fatigue data; thus, hindering adoption of AM to fatigue critical applications. This study investigates the effect of surface quality and sub-surface porosity on high cycle fatigue behavior of 17-4 precipitation hardening (PH) stainless steel (SS) fabricated using laser beam powder bed fusion (LB-PBF) process. Parts were fabricated in three conditions: net-shape (NS) specimens, oversized specimens, and cylindrical rods. The oversized specimens and cylindrical rods were, respectively, further shallow machined (SM) and deep machined (DM) to the dimensions and geometry of net-shape specimens. The population of defects was investigated via optical microscopy of polished sections, X-ray micro-CT scan analysis, and fractography of fracture surfaces after fatigue tests. The fatigue crack growth (FCG) properties were generated at three stress ratios of $R = -1$, 0.1, 0.7 to determine the Kitagawa-Takahashi diagram and propagation curve. The polished sections showed the presence of large sub-surface, close-to-surface pores in the NS specimens, while SM and DM conditions had smaller and more uniformly distributed porosity. Critical defects detected on the fracture surfaces were small pores in machined specimens, and relatively large surface irregularities in NS specimens. Machining process, both in SM and DM conditions, enhanced the fatigue performance of the material as compared to that of NS condition. However, in terms of level of machining allowance, no further enhancement in fatigue performance was observed for DM specimens as compared to that of SM ones. Fatigue assessment for both net-shape and machined conditions was obtained performing FCG simulations based on the typical surface features and volumetric defects. Simulation results yielded correct estimates for both net-shape and machined specimens.

1. Introduction

The various advantages of additive manufacturing (AM) techniques (e.g. fabricating complex geometries, functional component, cost effectiveness, etc.) are counterbalanced by some drawbacks, which hinder simple and cost-effective design, and qualification of critical load-bearing parts. Yadollahi and Shamsaei [1] reviewed the challenges of AM processes focusing on their fatigue performance. Untrustworthiness and uncertainty often observed in fatigue performance of additively manufactured parts were highlighted as the dominant challenge against their widespread industrial adoption in fatigue critical applications. In this regard, they declared that process-structure-property-performance relationships of different AM processes and material systems must be established to overcome these challenges.

Additively manufactured materials often show larger variability and lower repeatability as compared to the wrought counterparts due to two main criticalities of AM processes, i.e. volumetric defects and detrimental surface features caused by coarse surface finish [2,3]. The term "volumetric defect" refers to any process-dependent defect that can arise in any region of the material volume fabricated. As the position of such defects is random [4–6], they can occur in the middle of the specimen or in proximity of the surface. On the contrary, the term "surface feature" includes any process-dependent defect that only occurs on the outer surface or beneath it. On this base, one of the main

---

Nomenclature

a_i	initial crack depth
a_0	El-Haddad size parameter for cracks
C, n, p, q	coefficients of NASGRO equation
C_{th+}, C_{th-}	coefficients for FCG threshold determination
d	depth of surface features
f, A_0	Newman coefficients for crack closure determination
K_c	fracture toughness
N_f	number of cycles to failure
R	applied load ratio
Y	boundary correction factor for SIF calculation
α	constraint factor
$\Delta\sigma$	stress range
$\Delta\sigma_w$	fatigue limit stress range
$\Delta\sigma_{w0}$	fatigue limit in the absence of defects
ΔK	stress intensity factor range
ΔK_{th}	crack propagation ΔK threshold
$\Delta K_{th,lc}$	long cracks fatigue crack propagation ΔK threshold
$\Delta K_{th,1}$	effective ΔK_{th}
$\sqrt{area}$	Murakami's defect size parameter
$\sqrt{area}_0$	El-Haddad size parameter for defects

Acronyms

AM	additive manufacturing
CA	condition A
CT	computed tomography
DM	deep machined
FCG	fatigue crack growth
HCF	high cycle fatigue
LB-PBF	laser beam powder bed fusion
LEFM	linear-elastic fracture mechanics
LEVD	largest extreme value distribution
NS	net-shape
OM	optical microscopy
PH	precipitation hardening
SEM	scanning electron microscopy
SIF	stress intensity factor
SM	shallow machined
SS	stainless steel

concerns is the fatigue strength assessment of additively manufactured materials. Previous investigations have shown that fatigue properties in the presence of volumetric defects can be obtained applying fracture mechanics models, i.e. the Kitagawa-Takahashi diagram for fatigue limit assessment [7–10] plus FCG simulations [11,12] or fatigue approaches [8,13–15] for finite life estimation. Recently, Torries et al. [16] overviewed factors affecting the fatigue life (e.g. surface roughness, volumetric defects, and microstructure) as well as incorporation of such factors with various fatigue modeling methodologies (i.e. microstructure- and defect-sensitive models) to predict fatigue life of additively manufactured parts.

Regarding the surface condition, fatigue assessment is more complex due to strong influence of various process parameters (e.g., laser power, scanning speed, layer thickness, contouring strategy, build orientation) on the part's surface roughness [10,17–22]. Even if roughness measurements are often adopted to evaluate the surface quality of AM parts, various studies have demonstrated that common average or peak-to-valley measurements are not enough to obtain a robust correlation with fatigue life [10,21,23–25]. In some cases, this is because of extensive porosity detected below the surface, especially when contouring strategies are performed on parts produced via LB-PBF and is more exacerbate in down-skin surfaces. In fact, this usually happens when parts are fabricated inclined with respect to the building direction and without supporting structures (see Fig. 1), as the unmelted powder on which the down-skin surfaces are fabricated cannot dissipate heat as the wrought material [21]. Pegues et al. [19] investigated the surface roughness effect on the fatigue performance of LB-PBF Ti-6Al-4 V fabricated at 45° (i.e. diagonal with regard to the building direction). They have observed inferior fatigue performance for the specimens possessing higher down-skin surface roughness as compared to the ones with lower down-skin surface roughness. This is because crack initiation is highly sensitive to the surface roughness and asperities, even when subsurface pores are absent.

To consider the effects of net-shape surface condition, three major approaches are adopted in the literature: (i) the evaluation of the stress concentration induced by surface features [10,24,26–28]; (ii) estimating a fictitious (i.e. equivalent initial flaw size approach) crack representing the 'as-built' condition [14,29], and (iii) measuring the dimensions of surface features for applying 'short crack' fracture mechanics concepts [10,14]. If the adoption of crack concepts allows FCG calculations and it is essential for a structural assessment [30], the latter method has the advantage of allowing a competing-risk

assessment of surface features and volumetric defects in the Kitagawa-Takahashi diagram [7]. Such an analysis may be found critical in presence of severe volumetric defects, whose detrimental effects are competitive with surface notches [31] or surface roughness [1,32,33].

There have been some recent investigations on the mechanical properties of additively manufactured 17-4 precipitation hardening (PH) stainless steel (SS). PH stainless steels are chromium and nickel containing steels providing high strength, toughness, and corrosion resistance, which 17-4 PH SS is one of the most well-known grades of martensitic PH stainless steels. This material can exhibit a wide variety of strength and toughness properties due to precipitation hardening behavior activated by performing specific heat treatment procedures. As a result, 17-4 PH SS has been used in different industries such as aerospace, oil and petroleum, power plants, etc.

Nezhadfar et al. [34] studied the synergistic effects of surface condition and heat treatment on the fatigue behavior of LB-PBF 17-4 PH SS. They showed that solution heat treatment (i.e. condition A (CA)) prior aging, regardless of the surface condition, enhances the fatigue performance due to the formation of more homogenous microstructure in LB-PBF 17-4 PH SS. The effect of build orientation on the fatigue performance of LB-PBF 17-4 PH SS has been also investigated in [35] and a higher fatigue resistance for horizontally fabricated specimens as compared to the ones fabricated vertically is reported. This behavior has been attributed to the orientation of inter-layer defects with respect to the loading direction. In addition, the fatigue crack growth (FCG) behavior of LB-PBF 17-4 PH SS was found to be significantly influenced by heat treatment. Abnormal FCG behavior was observed to depend on the building orientation for non-homogenous microstructure with columnar grains. However, the building orientation was found not to affect the FCG behavior in homogenous microstructure [36].

Although various studies investigated the effect of surface machining on the fatigue performance of additively manufactured 17-4 PH SS, the effect of machining depth on the fatigue behavior has not been investigated. It is essential to understand how to improve the surface condition and how deep such treatments shall go to avoid any detrimental effect of sub-surface, close-to-surface defects on the fatigue behavior of LB-PBF 17-4 PH SS. At the same time, robust non-destructive inspection methodologies must be selected and standardized. Therefore, the present study aims to thoroughly evaluate the effect of surface features and sub-surface defects on the fatigue resistance of LB-PBF 17-4 PH SS by removing different depths of material via machining, and to suggest a simple but effective fatigue strength and life
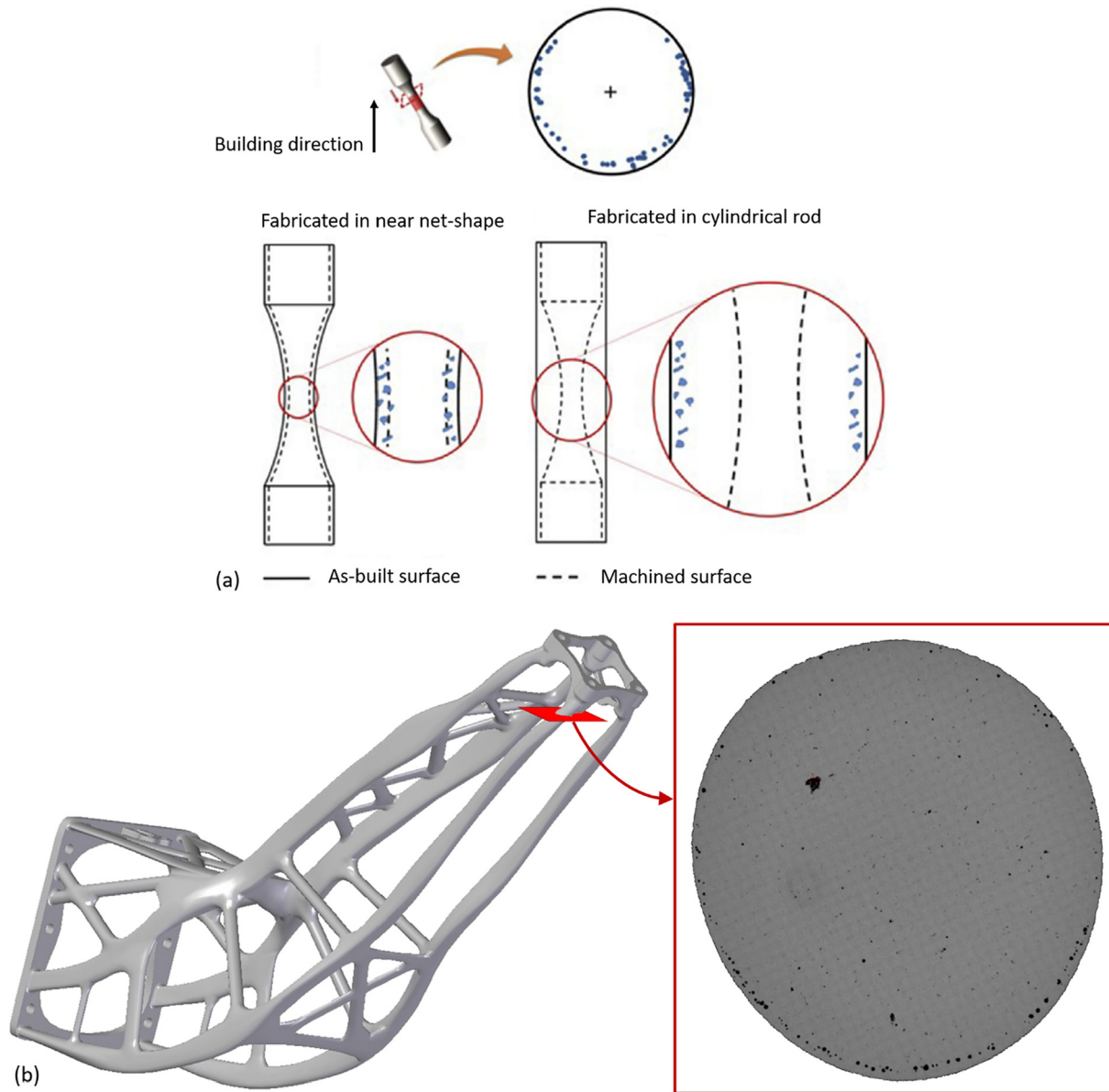
Fig. 1. Typical sub-surface features in net-shape parts: (a) sub-surface porosity generated by the LB-PBF process in net-shape or machined specimens (adapted from [1]); (b) sub-surface porosity in the down-skin region of an inclined AlSi10Mg part produced without supports (adapted from [7]).

estimation methodology, extendable to other AM processes and material systems.

2. Material and experiments

2.1. Material and specimen fabrication

Argon atomized 17-4 PH SS powder with the chemical composition listed in Table 1 was used to fabricate specimens. The particle size distribution was reported to be within the range of 15–45 μm by the manufacturer, LPW Technology Inc.

Specimens were fabricated in the vertical orientation using EOS

Table 2
LB-PBF process parameters for 17-4 PH SS recommended by EOS.

Laser Power (W)	Scanning speed (mm/s)	Hatching space (μm)	Layer thickness (μm)
220	755.5	100	40

M290 machine. Fabrication of all the specimens were carried out under nitrogen (N_2) shielding gas using process parameters listed in Table 2 suggested by EOS. In addition, a post-contour was applied in the fabrication process with the speed of 400 mm/s, power of 160 W, and width of 80 μm.

Table 1
Chemical composition of 17-4 PH SS provided by LPW Technology Inc.

	C	Cr	Ni	Cu	Mn	Si	Nb	Mo	N	O	P	S	Fe
(Wt. %)	0.01	15.60	4.03	3.89	0.24	0.29	0.33	< 0.01	0.01	0.05	0.004	0.003	Bal.

The build layout is shown in Fig. 2, which consisted of 10 net-shape (NS) fatigue specimens, 10 oversized parts to be further machined to final dimensions of fatigue specimens, and 8 FCG specimens. Dimensions for fatigue specimens before and after machining are provided in Fig. 3a.

Ten specimens were directly manufactured to the net-shape (NS) geometry, 5 parts were fabricated oversize, and 5 parts were cylindrical. The oversize and cylindrical parts were further machined to the same geometry as NS ones, which is highlighted in Fig. 3a in red. Accordingly, by having different machining allowance in the gage section (i.e. shallow machining (SM) for oversize and deep machining (DM) for cylindrical parts), it could be evaluated whether a relatively small material removal from the surface could be enough to eliminate any detrimental effects of surface roughness and sub-surface, close-to-surface pores. For the SM group, the machining allowance was an overall reduction of 1 mm in the gauge diameter (i.e. 0.5 mm surface removal), while there was an overall reduction of 3 mm (i.e. 1.5 mm surface removal) in the gage diameter of DM ones.

Eight single-edge bending geometries for FCG specimens were machined out of 110 mm × 26 mm × 11 mm parallelepipeds. The final geometry of these specimens is depicted in Fig. 3b. A 100 μm-thick micro-notch was introduced in the center of these specimens by electro-discharge machining (EDM) to promote crack initiation with limited stress concentration effects (see detail A in Fig. 3b).

All specimens were subjected to the CA-H1025 heat treatment procedure proposed as an appropriate heat treatment for the LB-PBF 17-4 PH SS [34]. This heat treatment procedure consists of two steps; first, solution heat treating (i.e. Condition A (CA)) at 1050 °C for half an hour followed by air cooling to the room temperature. Second, heat treating at 552 °C for four hours followed by air cooling to room temperature. All the heat treatment procedures were performed in an inert atmosphere of Ar. For this condition, an ultimate tensile stress of 1167 MPa, a yield stress of 1140 MPa, and a true fracture strain of 0.30 are expected for CA-H1025 LB-PBF 17-4 PH SS [37].

Surface roughness measurements were performed in the gauge volume of NS specimens along the axial direction. The results summarized in Table 3 refer to one of the specimens investigated, while equivalent results were obtained on the other specimens. The surface roughness was evaluated onto 4 evaluation lengths of 10 mm in terms of Ra (arithmetical mean roughness), Rz (maximum height), Rp (maximum profile peak height), Rv (maximum profile valley depth), and Rt (total height).

2.1.1. Microstructure

Fig. 4a and 4b depict the microstructures of the NS specimens on the perpendicular plane to the build direction in the non-heat treated and the heat treated conditions. The contour layer is observed in non-heat treated condition, which is composed of fine equiaxed grains (Fig. 4a). However, it can be seen in Fig. 4b the microstructure is homogenized after performing the CA-H1025 heat treatment. Accordingly, due to the microstructure homogenization obtained after performing CA-H1025 heat treatment, no significant differences are expected among the three NS, SM, and DM conditions, as seen in Fig. 4c–4e, respectively. Therefore, the effect of microstructure on the fatigue performance of the material in three different conditions (i.e. NS, SM, and DM) is eliminated to study the effect of sub-surface pores as well as surface roughness.

2.2. Porosity measurements

2.2.1. X-ray micro-CT

X-ray micro-CT was performed with a commercial machine in microfocus tube mode. The main parameters adopted for the analysis are reported in Table 4.

2.2.2. Polished section

Specimens from each condition (NS, SM, and DM) were cut transversely in the gauge length section (i.e. parallel to the building direction), cold mounted, and the surfaces were prepared for metallography. Specimens were progressively ground using different grit sandpapers (320–2500), and eventually polished to a mirror-like surface using 0.05 μm MasterPrep Alumina solution on a ChemoMet pad. A Keyence VHX-6000 digital microscope was used to observe and measure the porosity size and distribution using differential contrasts method. Specimens were progressively polished, the porosity size and distribution were analyzed in different depths, and eventually the average values were obtained.

2.3. Fatigue testing and fractography

Axial fatigue tests were performed using an axial Rumul resonance machine Testronic applying frequency of 80 Hz. Fatigue specimen geometry and dimensions are provided in Fig. 3a. Specimens were tested in the high cycle fatigue (HCF) regime to evaluate lives above 10^5 cycles and the fatigue limit region. The run-out level was set to 10^7 cycles. The tests were stopped when a variation in the applied frequency was measured above 2 Hz, which is caused by a decreased stiffness of the specimen. When this happened, a crack was always visible in the gauge region and the specimen was considered failed. The specimens that survived 10^7 cycles were re-tested at larger stress levels after verifying that no visible damage had occurred.

Regarding FCG testing, three specimens were pre-cracked in compression for 6×10^6 cycles on an axial Rumul Testronic resonance machine. A frequency of 80 Hz was adopted with a stress ratio of
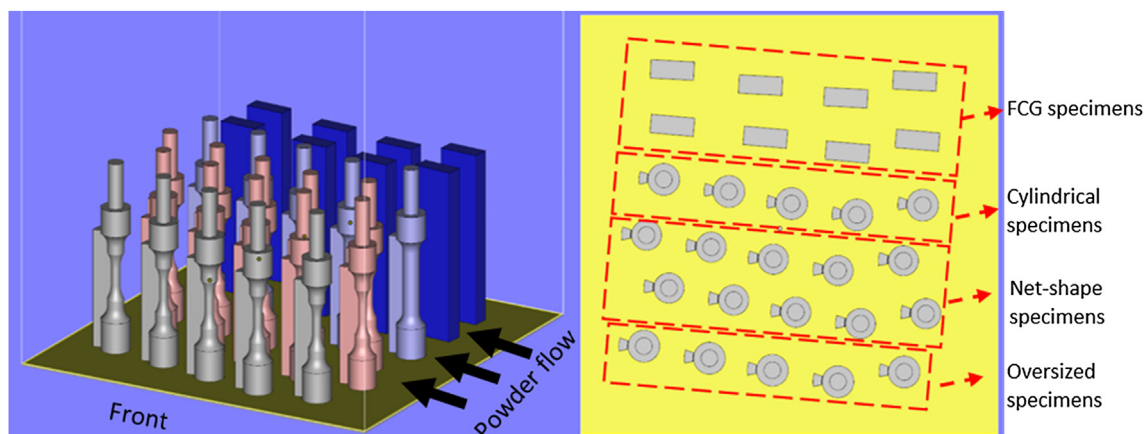

Fig. 2. LB-PBF build layout, showing net-shape (NS), oversize, and cylindrical specimens for fatigue testing as well as parallelepiped specimens for FCG testing.
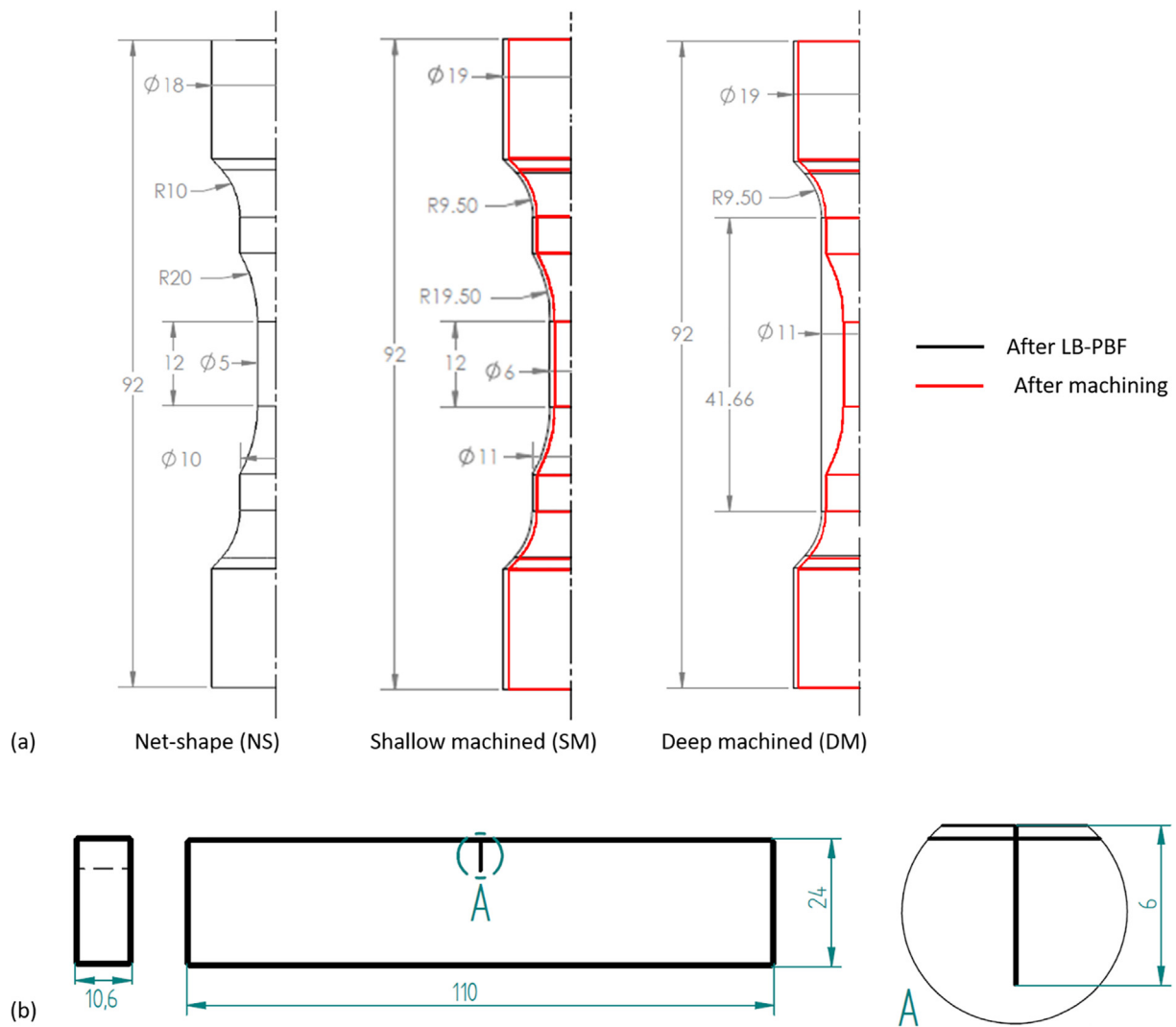
Fig. 3. Drawing of specimens: (a) uniaxial fatigue according to ASTM E466 [39], geometries before machining (in black) and after machining (in red); (b) single-edge bending (SE(B)) FCG after machining according to BS ISO 12108 [40]. (For interpretation of the references to colour in this figure legend, the reader is referred to the web version of this article.)

Table 3

Surface roughness measurements according to ISO 4288:1996 [38]. Ra and Rz values are averaged on the four evaluation lengths, while minimum and maximum values are reported for Rp, Rv, and Rt.

Ra (µm)	Rz (µm)	Rp (µm)	Rv (µm)	Rt (µm)
7.2	87.6	24.6–47.3	49.6–59.4	79.9–96.9

$R = 10$. The specimen geometry is depicted in Fig. 3b. The aim of this step is to introduce a closure-free pre-crack, which allows starting the FCG tests applying relatively small loads. The length of the pre-cracks was measured using the optical microscope on the two sides and resulted symmetric with a length of 80 ± 20 µm. After compression pre-cracking, fractomat krak gages were applied on the two sides of the specimens to measure crack growth. Four-point bending tests were then performed on a Rumul Cracktronic resonance test rig and consisted in a short crack stabilization with constant amplitude load, followed by a ΔK-decreasing test. Three tests were performed to investigate the material response at three stress ratios, i.e. $R = 0.7$, $R = 0.1$ and $R = -1$. After determining $\Delta K_{th,lc}$, the tests performed at positive stress ratios were continued applying a constant amplitude moment to evaluate the crack growth rate in the Paris region.

To determine the major cause of the fatigue failure, i.e. the feature from which the fatigue crack was originated, fractography analysis was performed on all fracture surfaces via Keyence VHX-6000 digital microscope and scanning electron microscope Zeiss EVO 50. The size of such features was then measured utilizing $\sqrt{area}$ parameter [41].

3. Experimental results

3.1. X-ray micro-CT

Defect analysis was performed on all specimens using VG Studio Max software using recommended settings. No pore was detected with enough confidence to state no false positive results were obtained. The same output was obtained by manually changing the parameters of the defect analysis. However, a few sub-surface spherical pores were detected looking at the reconstructions of the NS specimens. The dimension of such pores, shown in Fig. 5, was estimated to be approximately 80 µm in diameter or 70 µm in terms of $\sqrt{area}$. However, no defects were detected in SM and DM specimens.

3.2. Analysis of polished sections

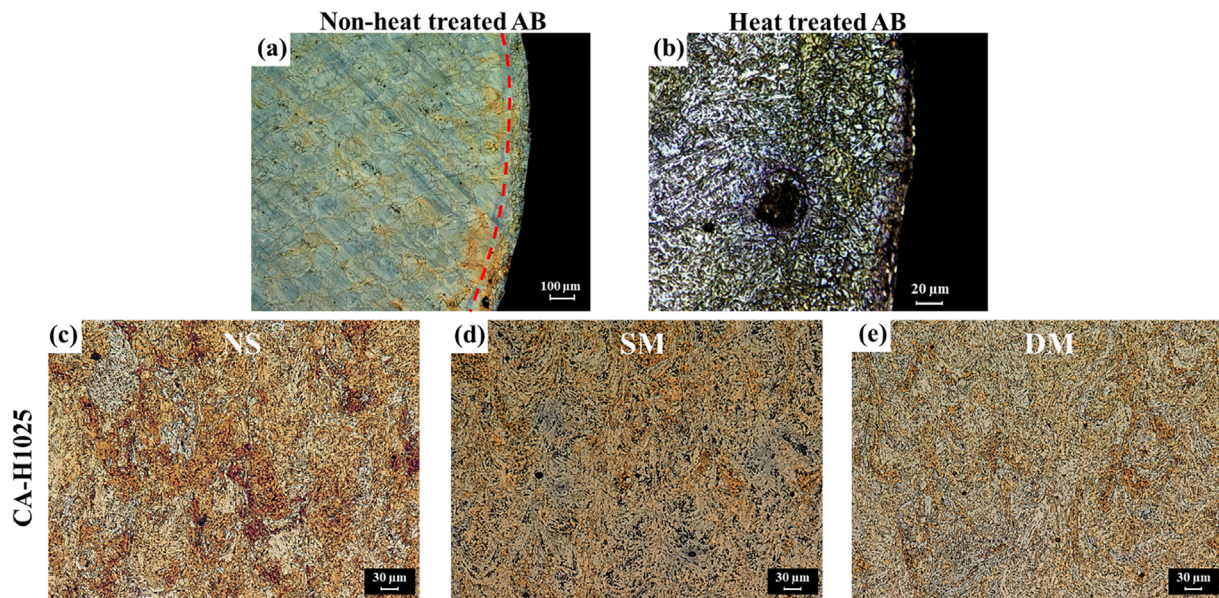The analysis of polished sections in the gage section of specimens

Fig. 4. Overview of microstructures before and after CA-H1025 heat treatment.

Table 4
Parameters adopted for X-ray micro-CT analyses.

Resolution (µm)	Voltage (kV)	Intensity of current (µA)	Focus-object distance (mm)	Focus-detector distance (mm)	Number of projections	Integration time (s)
21	200	200	120	800	1440	1.50

shown in Fig. 6 highlighted the presence of relatively large sub-surface pores in NS specimens. The largest pore size measured had a $\sqrt{area}$ of 55 µm (see Fig. 6a). It is worth noting that only the polished area close to the periphery surface of specimens are shown herein, however, the porosity analysis is carried out for the thorough area in the gage section. Fig. 6b shows the polished section of a machined specimen. It was found out that removing the surface by 0.5 mm (i.e. in the case of SM specimens) would eliminate the large pores close to the surface. Similarly, no large pores were found close to the surface of the DM specimens due to deeper machining.

The largest pore measured through 2D analysis (i.e. 55 µm) is slightly smaller than the findings of X-ray micro CT and fracture surfaces in NS specimens (i.e. 60–80 µm). This is due to the fact that the size of the largest and most critical defect depends on the volume of material investigated [4,25]. Analyzing a large amount of material is simple adopting a 3-D technique as X-ray micro CT (the specimen gage volume plus grips were investigated in a unique scan), while a large experimental effort is needed to investigate similar volume via 2-D measurement methods as the analysis of polished sections [25]. Regarding the analysis of fracture surfaces, fatigue testing is another simple way of investigating large material volumes with limited effort, as fatigue failure is naturally caused by the largest defect in the gage volume [41]. A further limitation of polished sections is that pores are more likely sliced not in the middle of the cross-section, which causes a systematic underestimation of the defect size.

Fig. 7 shows the distributions of pores for the three conditions, which were measured analyzing a polished area of approximately 40 mm^2 and setting a lower bound for the pore size to 10 µm to take into account in analysis. The defect density (i.e., the number of defects per unit volume) is minimum for SM specimens (7 defects/mm^2), while
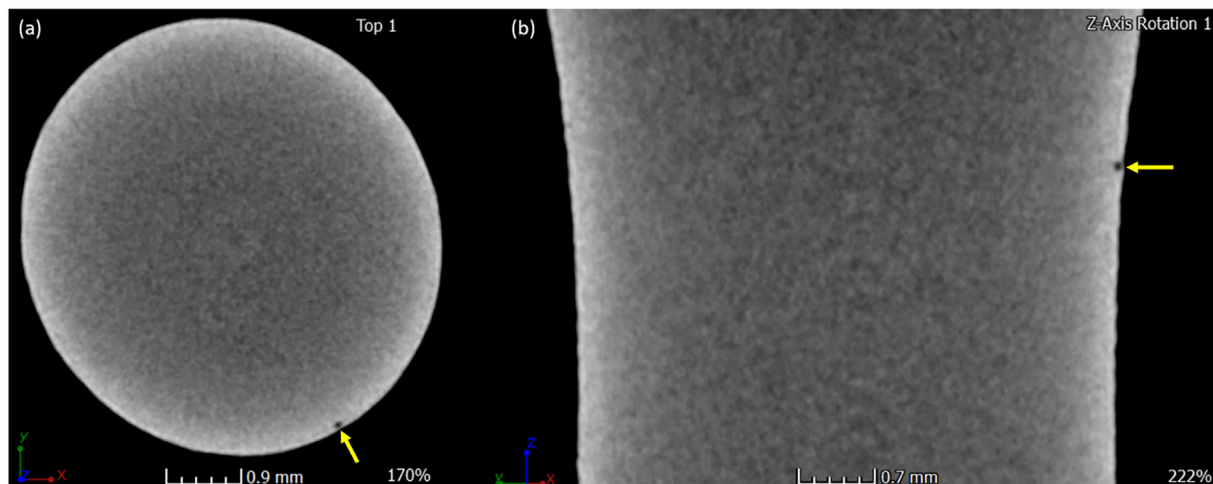

Fig. 5. Example of sub-surface, and close-to-surface pores detected via X-ray micro-CT. The arrows show its position in (a) radial and (b) longitudinal directions.
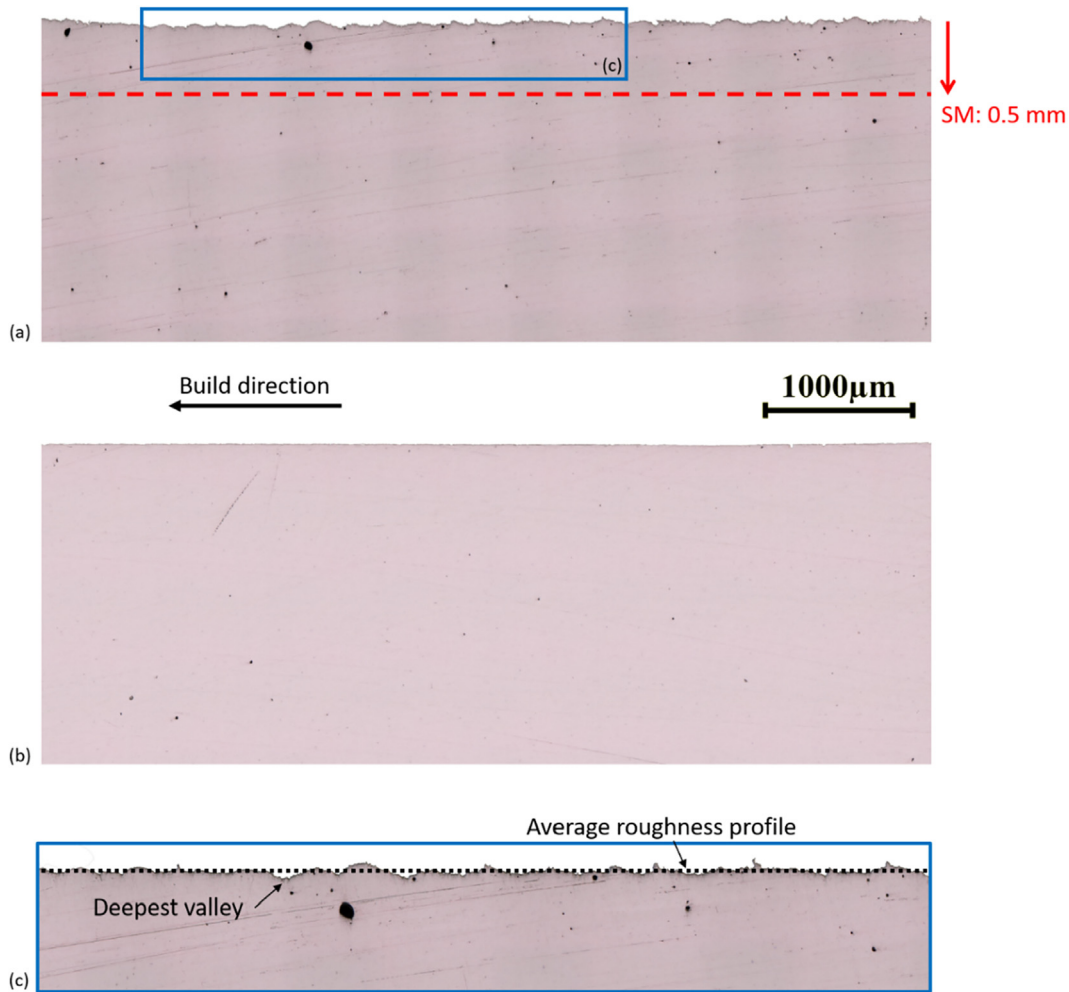
Fig. 6. Examples of polished sections for: (a) NS; and (b) SM specimens (similar results were obtained for DM specimens); (c) detail of roughness profile for NS condition.
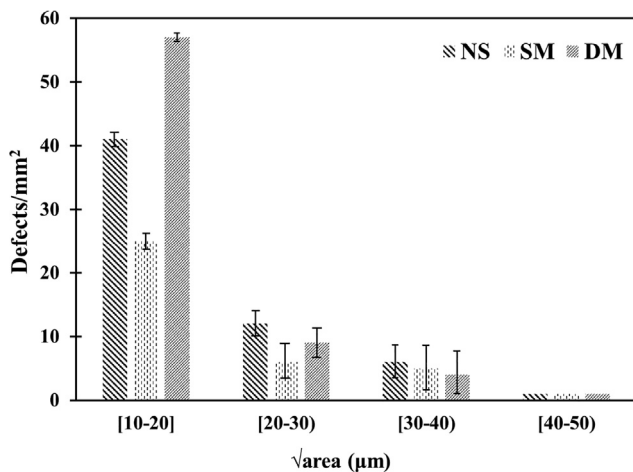

Fig. 7. Porosity size distribution obtained from polished sections.

the increase of cross section of DM specimens appears to promote the formation of more pores (22 defects/mm^2). A defect density of 14 defects/mm^2 was registered in NS specimens. It has been shown that the porosity size and distribution will be influenced by the part geometry [42]. As the difference in cross section is small with respect to the SM geometry, not much variation in porosity level are expected. However, the reason for this increment appears to be the larger concentration of

pores in proximity of the outer surface, which was machined away in the SM specimens (see Fig. 6a). Despite the differences in the defect density, the three defect distributions appear to be consistent among each other, as the average defect size resulted in the range 14–15 μm. Note that the number of large critical pores was very small, as only two pores larger than 30 μm were detected, however, both in the proximity of the surface in the NS specimens.

In addition to such pores, the NS surface condition also contains deep valleys due to the surface roughness, which can introduce stress concentrations and negatively affect the fatigue performance of the material [10,17,26,43]. For the present material, the maximum valley depth measured on the polished sections was approximately 65 μm (see Fig. 6a).

As was mentioned earlier, the large sub-surface pores were all removed by machining in both SM and DM specimens, while the size and number of remaining pores in both machined conditions (see Fig. 6b) were similar to those found in NS specimens. This demonstrates that removing the outer layers of material allowed obtaining a stable and repeatable quality despite the difference in the three geometries fabricated. Considering machined conditions, the analysis of polished sections resulted consistent with the crack initiating pores found on the fracture surfaces, as the largest pores detected were within the same range of approximately 22–26 μm (i.e. $\sqrt{area}$) reported in Section 3.4.

3.3. FCG tests

Table 5 reports the FCG threshold for long cracks ($\Delta K_{\text{th,lc}}$) determined via ΔK-decreasing FCG tests.

The FCG behavior was described by standard fracture mechanics approaches using the NASGRO software v8.2 [44]. Crack closure effects were accounted via the Newman's opening function (f) [45] adopting the predefined settings, i.e. a constraint factor of $\alpha = 2.5$ for crack propagation and $\alpha = 2$ for the threshold region, and a constant value of 0.3 for the ratio between the maximum stress and the flow stress. The dependence of ΔK_{th} on the stress ratio was described using Eqs. (1) and (2):

$$\Delta K_{\text{th}} = \Delta K_{\text{th,1}} \left[\frac{1-R}{1-f} \right]^{(1+RC_{\text{th+}})} / (1-A_0)^{(1-R)C_{\text{th+}}} \quad \text{for } R \geq 0 \quad \text{and} \tag{1}$$

$$\Delta K_{\text{th}} = \Delta K_{\text{th,1}} \left[\frac{1-R}{1-f} \right]^{(1+RC_{\text{th-}})} / (1-A_0)^{(C_{\text{th+}}-RC_{\text{th-}})} \quad \text{for } R < 0 \tag{2}$$

where $\Delta K_{\text{th,1}}$ is the effective FCG threshold, A_0 can be determined via the Newman model for crack closure, and the coefficients $C_{\text{th+}}$ and $C_{\text{th-}}$ can be determined via best-fit to the experimental threshold data.

Fatigue crack growth at different propagation regimes was described by fitting a NASGRO equation on the experimental data to determine the four parameters (C, n, p, q):

$$\frac{da}{dN} = C \left[\left(\frac{1-f}{1-R} \right) \Delta K \right]^n \frac{\left(1 - \frac{\Delta K_{\text{th}}}{\Delta K} \right)^p}{\left(1 - \frac{K_{\max}}{K_c} \right)^q} \tag{3}$$

Table 6 reports the values of all the parameters obtained from simulations. As no fracture toughness (K_c) data was available, no unstable propagation was considered by setting $q = 0$. The best fit obtained is depicted in Fig. 8.

3.4. Fatigue tests

Fig. 9 depicts stress-life fatigue data of the three batches (i.e. NS, SM, and DM conditions). For comparison, fatigue results of LB-PBF 17-4 PH SS fabricated under Ar shielding gas adopted from [34] are also included in this figure as Ref. NS and Machined. It is worth mentioning that reference specimens were subjected to the same heat treatment procedure (i.e. CA-H1025).

The machined specimens investigated in this study yielded slightly longer fatigue lives than the reference data (from specimens fabricated in Ar environment), while slightly shorter lives were recorded for NS specimens fabricated in N_2 environment for this study. Moreover, regardless of surface condition, more experimental variability was observed in N_2 data than the Ar data adopted from the previous investigation [34]. Both shallow-machining and deep-machining resulted in specimens to exhibit a nearly constant improvement of 200–300 MPa in the HCF region as compared to the NS specimens. A non-negligible scattering is evident throughout all the S-N datasets. Most of the experimental variability in additively manufactured materials is usually caused by defects. Therefore, there is a need to capture the effect of internal and surface defects on the fatigue strength and life by applying a damage-tolerant approach capable of considering short cracks effects, i.e. Kitagawa-Takahashi diagram [46].

The fatigue limit for the NS condition was evaluated performing a staircase test procedure with a 25 MPa step. According to the Dixon and Mood method [47], the fatigue strength of the NS specimens at 5×10^6 cycles found to be 221 MPa, with a coefficient of variation of 4.5%. The fatigue data were fitted according to ASTM E739 [48]. The scatter of the data points was evaluated accordingly and resulted $\sigma_{\text{logN}} = 0.258$ for machined specimens and $\sigma_{\text{logN}} = 0.257$ for NS specimens. This value is in line with the results obtained in Ref. [11] for AlSi10Mg and it is consistent (considering that the data of different batches were included)

with the indication of DVNGL-RP-C210 [49] that mentions $\sigma_{\text{logN}} = 0.2$ for welded components.

3.5. Analysis of fracture surfaces

Fig. 10a shows the typical fracture surface of NS fatigue specimens investigated via scanning electron microscopy (SEM). The failure occurred in correspondence of loose powder (i.e. partially fused) particles and inhomogeneous regions along the outer layer of the specimens, similar to those reported by Ngnekou et al. [43] for NS AlSi10Mg. The coarse surface quality acts as a long and shallow crack having a depth of around 60–80 μm, i.e. similar to the width of the post-contour and maximum valley depth (see Section 3.2), and semi-length on the surface around 350–450 μm. In one case, presence of a sub-surface pore with a diameter of 67 μm right below this outer layer has probably increased the detrimental effects of surface roughness [26,50] (see Fig. 10b). The size and position of this pore is consistent with those detected via X-ray micro-CT scan (see Fig. 5). Finally, the NS specimen tested at a maximum stress of 400 MPa (see Fig. 9) experienced multiple crack initiation sites, which is probably the reason why it has tolerated less cycles than expected.

Examples of typical fracture surfaces of machined specimens are depicted in Fig. 11. In all cases, a surface or sub-surface, but very close to surface, spherical pore was found to be responsible for the crack initiation. The dimension of critical pores was seen to be consistent throughout all the machined specimens, with diameters within the range of 20–30 μm. This size is consistent with the findings of Carneiro et al. [51] for a similar material fabricated by LB-PBF in Ar environment.

Empirical relationships were adopted to evaluate the effective defect size for sub-surface pores. According to Murakami [41], the stress intensity factor (SIF) for a sub-surface defect can be correctly evaluated by measuring its $\sqrt{\text{area}}$ considering also the ligament between the defect and the outer surface (as depicted in Fig. 11b).

4. Discussion on experimental results and fatigue life prediction

The investigations performed have demonstrated the important reduction in fatigue strength for NS specimens caused by the presence of deep valleys due to their coarse surface finish. At the same time, failure in some NS specimens was influenced by few large pores (approximately 80 μm in diameter) having the center of gravity at 80–100 μm depth from the outer surface. Since the volumetric defects and surface roughness hypothetically behave as short cracks, modelling the competition between such defects requires utilizing a fracture mechanics approach. Under the commonly adopted hypothesis that both defect types behave as short cracks, the fatigue limit corresponds to the threshold condition for cracks/defects. Adopting Murakami's formulation, the SIF of a defect can be evaluated as

$$\Delta K = Y \Delta \sigma \sqrt{\pi \sqrt{\text{area}}} \tag{4}$$

where $\Delta \sigma$ is the applied stress range, while the boundary correction factor is set to $Y = 0.65$ for surface defects and $Y = 0.5$ for internal defects.

In the case of volumetric defects, the initial size of the crack is considered simply as the $\sqrt{\text{area}}$ of the projected defect one the loading plane [41]. However, presence of surface valleys entangles determination of defect size. Knowing the depth, d, of such features, a

Table 5
Results of the FCG tests performed (crack growth rates in mm/cycle, ΔK in MPa m$^{0.5}$).

R	0.7	0.1	-1
$\Delta K_{\text{th,lc}}$(MPa m$^{0.5}$)	2.47	4.06	7.27

Table 6
Parameters of the NASGRO equation fitted on the experimental data (ΔK in MPa m$^{0.5}$, crack propagation rate in mm/cycle).

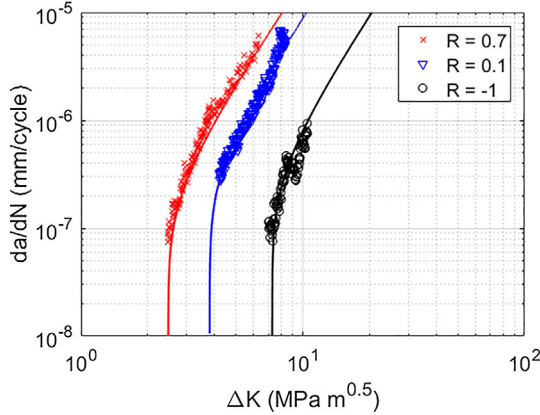| C	n	p	q	ΔK_1	C_{th+}	C_{th-}
2.6310^{-6}	2.94	0.50	0	67.77	0.67	0.00

Fig. 8. NASGRO fit to the experimental FCG data obtained via NASGRO software.
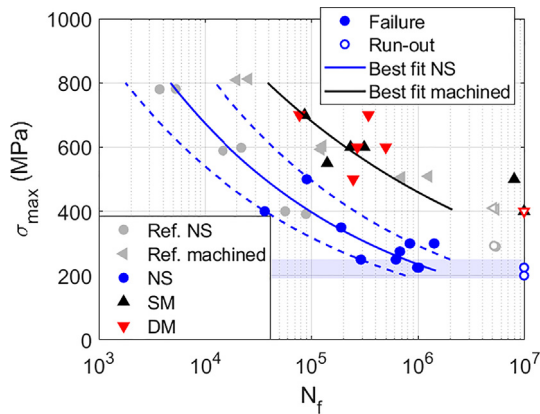
Fig. 9. Stress-life fatigue data representing the effect of machining allowance on the fatigue performance of LB-PBF 17-4 PH SS and their comparison with data adopted from [34]. The dotted blue lines represent the 95% scatter band of the experimental data for NS specimens. (For interpretation of the references to colour in this figure legend, the reader is referred to the web version of this article.)

conservative estimate of the size can be obtained by the empirical relation

$$\sqrt{\text{area}}_{NS} \cong d\sqrt{10} \tag{5}$$

which is valid for shallow 2D cracks and surface roughness [41,52]. Accordingly, the initial crack size for NS specimens was estimated to be approximately $190-250$ μm, considering the measured depth to be within the range of 60–80 μm (see Fig. 10). This range of dimensions is comparable to the depth of the maximum measured surface valley, which controls the fatigue strength of machined surfaces [52] and has been successfully adopted for 'as-built' surfaces [53,54].

Being considerably larger than the dimension of sub-surface pores, this size estimate agrees with the experimental evidence of most severe effect of surface-related features on the fatigue behavior of NS specimens.

4.1. Kitagawa diagram

The effect of short cracks on the fatigue limit was evaluated in the Kitagawa-Takahashi diagram described via the El-Haddad model [55] adopting the $\sqrt{\text{area}}$ parameter [7]:

$$\Delta\sigma_w = \Delta\sigma_{w0}\sqrt{\frac{\sqrt{\text{area}}_0}{\sqrt{\text{area}}_0 + \sqrt{\text{area}}}} \tag{6}$$

The El-Haddad size parameter for fully-reversed loading ($\sqrt{\text{area}}_0$) was defined as

$$\sqrt{\text{area}}_0 = \frac{1}{\pi}\left(\frac{\Delta K_{th,lc}}{Y\Delta\sigma_{w0}}\right)^2 = 9\mu\text{m}, \tag{7}$$

where $Y = 0.65$ is Murakami's boundary correction factor for surface defects, $\Delta K_{th,lc} = 7.27$ MPa m$^{0.5}$ is the long cracks propagation threshold (see Table 5), while the estimate of the fatigue limit in the absence of defects was evaluated as the stress value corresponding to a plastic deformation of 0.05% in the stabilized cyclic curve [56]. As no data on the cyclic behavior with extensive plastic deformation were available for the material under investigation, a value $\Delta\sigma_{w0} = 2130$ MPa was evaluated from the monotonic curve [34]. This is expected to be a slightly conservative assumption, as the same material subjected to similar heat treatment (i.e. CA-H900) was seen to experience cyclic hardening [35], which is a common behavior of stainless steels.

Fig. 12a shows the Kitagawa-Takahashi diagram reporting the experimental points of the specimens tested in the three conditions, i.e. NS, SM, and DM. The model yields correct results, as all failures except for one NS specimen lay above the El-Haddad line, and all run-outs lay below. Considering the NS condition, the simple defect size estimation by Eq. (5) resulted in an effective description of the stress range limit. Note that a simple assessment based on LEFM yields correct estimates for defect sizes larger than 100 μm (i.e., for the present material in the NS condition). On the contrary, an LEFM-based assessment for a similar defect size would provide non-conservative estimates of the limit stress or SIF range when investigating other materials (e.g., AlSi10Mg [7,11], Ti-6Al-4V [7,57], and In718 [8]). This is because high-strength materials are more sensitive to defects, which means that even defects with smaller size can affect the fatigue strength.

When cracks (or defects) are present inside the material, the concept of fatigue limit ($\Delta\sigma_w$) is equivalent to that of crack propagation threshold (ΔK_{th}). In fact, the material experiences infinite fatigue life when the most critical crack does not have enough energy to start propagating. Substituting the El-Haddad model from Eq. (6) inside Eq. (4), the Kitagawa diagram can also be depicted in terms of SIF threshold (see Fig. 12b) as

$$\Delta K_{th} = \Delta K_{th,lc}\sqrt{\frac{\sqrt{\text{area}}}{\sqrt{\text{area}}_0 + \sqrt{\text{area}}}} \tag{8}$$

4.2. FCG simulations

NASGRO v8.2 [44] was used in this study to simulate the elastic FCG behavior for all fatigue tests. The crack case selected was semi-elliptical surface crack in solid cylinder (SC07) subjected to uniaxial fully-reversed loading. For every specimen tested in both NS and machined conditions, the initial crack size was defined so that its area was equivalent to that of the critical feature detected on the fracture surface. Considering a semi-circular crack, such equivalence is expressed as

$$a_i = \sqrt{2/\pi}\sqrt{\text{area}}, \tag{9}$$

where a_i is the initial depth of the surface crack considered in NASGRO.

A user-defined material was created based on the static and FCG data obtained. The NASGRO equation (Eq. (3)) was adopted to evaluate the FCG rate, whose parameters were obtained by best-fit of experimental data (see Table 6). NASGRO automatically stopped the
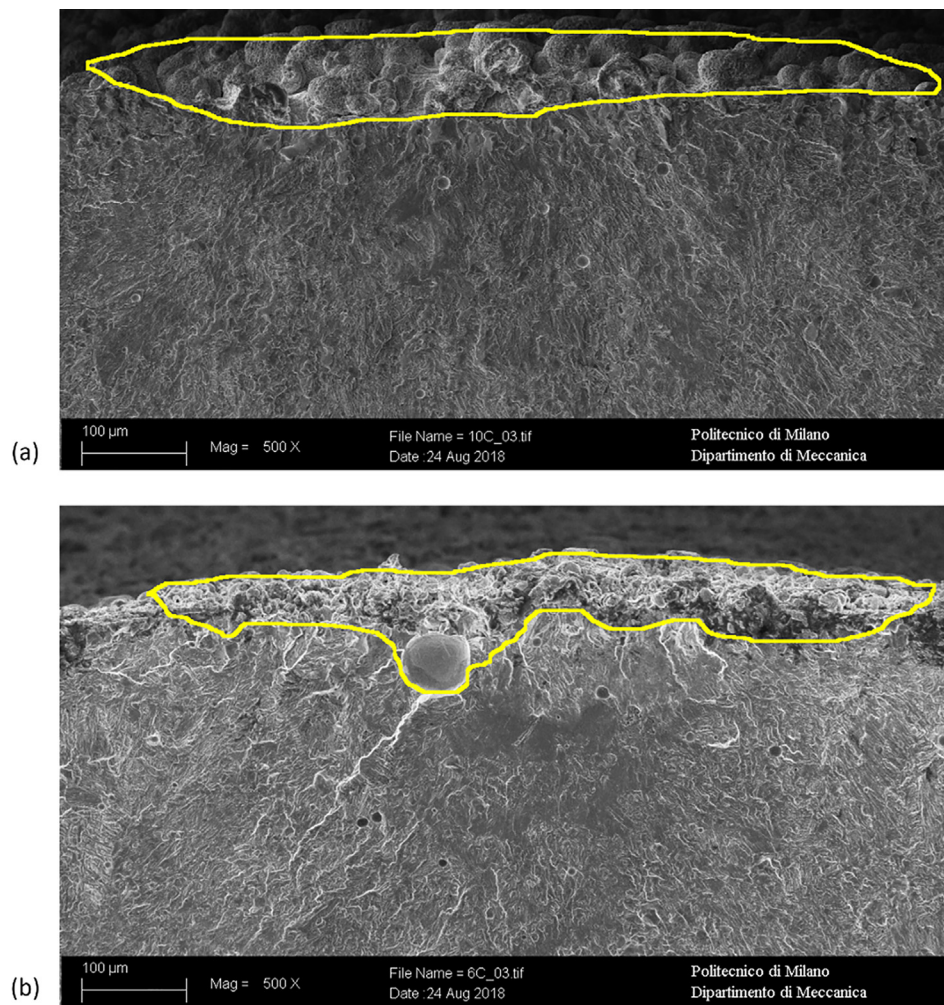
Fig. 10. Examples of typical fracture surfaces for the NS condition: (a) a specimen fractured after 6.22×10^5 cycles subjected to a stress amplitude of 250 MPa; and (b) a specimen fractured after 7.42×10^5 cycles subjected to a stress amplitude of 300 MPa showing a sub-surface pore with 65 μm diameter.

simulation when the net-section stress (i.e., the stress applied to the remaining uncracked section) exceeded the flow stress, which in NASGRO is defined as the arithmetical average between the yield strength and the ultimate tensile strength. The FCG threshold for short cracks was obtained from that of long cracks according to the Kitagawa-Takahashi diagram determined in Section 4.1. This was done using the NASGRO software, which adopts the same El-Haddad formulation by calculating $\Delta K_{th,1}$ in Eqs. (1) and (2) according to Eq. (8). The El-Haddad parameter was re-calculated using Eq. (9) from the $\sqrt{area}_0$ value determined in Section 4.1 and resulted in $a_0 = 7$ μm.

A lower bound fatigue life assessment was determined by considering an initial crack having the same area of the largest defect measured on the fracture surface, i.e. a crack depth $a_i = 29$ μm for SM and DM conditions and $a_i = 180$ μm for NS specimens. The results obtained are depicted in Fig. 13 in terms of number of cycles to failure and compared with the experimental fatigue stress-life fatigue data. The life assessment resulted appropriate in all cases except for one NS specimen that experienced multiple crack initiation sites.

4.3. Final remarks

The analyses performed in this study have demonstrated the applicability of fracture mechanics methods for the estimation of fatigue strength and finite life of 17-4 PH SS produced by LB-PBF. According to this approach, the problem of determining the endurance limit or fatigue life for AM materials becomes the ability to determine the type,

size, and location of the most critical defect. As in most cases fatigue failure of AM parts originates from surface or subsurface regions, surface treatments or machining can be adopted to remove or mitigate the effect of detrimental defects. Therefore, the choice of the best surface treatment or machining allowance is subordinate to the understanding of the failure mode of the material in the particular condition.

When fatigue specimens are available, the size and type of the critical feature, although destructively, can be directly identified from the fracture surface analysis. Considering materials in machined conditions or subjected to beneficial surface treatments, the failure is driven by volumetric defects. The size of these defects can be determined via deterministic non-destructive evaluation of the particular specimen under investigation or via statistical approaches suitable for estimating the critical defect size based on the average quality of the batch (i.e., approaches based on statistics of extremes [4]).

In general, surface features and volumetric defects compete on initiating the fatigue crack, and therefore, their criticality should be evaluated against each other. An effective estimation of the size of critical surface features for NS specimens was obtained by measuring the size of the deepest valley on polished sections (see Fig. 6c) and considering this size as the depth of a shallow crack. A simpler and more conservative assessment of the depth of such surface cracks can also be evaluated considering a worst-case scenario in which the depth of the 2D surface crack can be evaluated as the width of the contour layer, i.e. 80 μm. Fig. 14 shows a simplified schematic of geometric surface inaccuracies generated during the process as well as the position
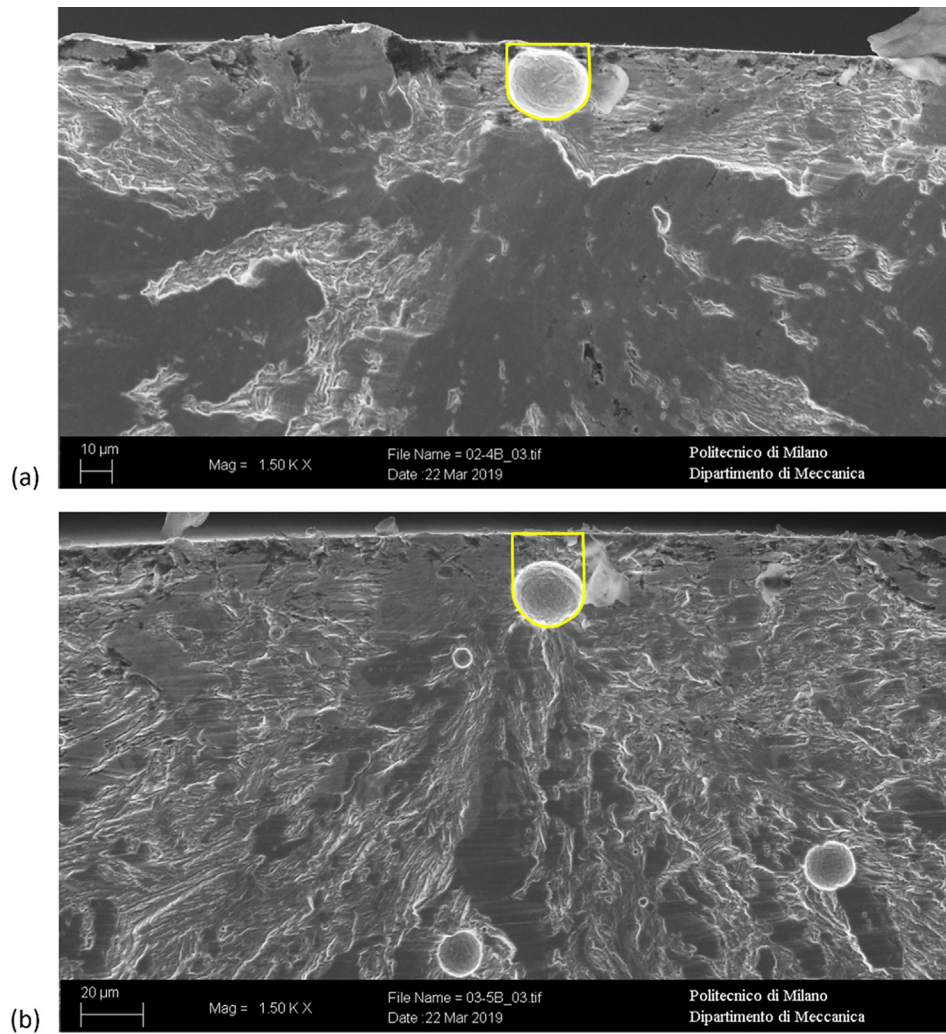
Fig. 11. Examples of typical fracture surfaces for the machined conditions: (a) a SM specimen fractured after 2.33×10^5 cycles subjected to a stress amplitude of 600 MPa; and (b) a DM specimen fractured after 3.42×10^5 cycles subjected to a stress amplitude of 700 MPa.

of sub-surface porosity with respect to the contour layer.

Considering this size plus the dimension of large sub-surface pores, it can be estimated that both detrimental features can be eliminated by removing at least 150–200 μm by machining or other processes (e.g., chemical or electrochemical milling, hirtisation). In fact, no failures caused by such features were recorded in either the SM (500 μm machining allowance) or in the DM (3000 μm machining allowance) specimens. In these conditions, cracks originated from smaller

volumetric defects that accidentally fell close to the surface after machining the external surface. Similar considerations should be given to the significant depth to be attained via other post-processing surface treatments aimed at decreasing the depth of the valleys and introducing compressive residual stresses (e.g., shot peening, vibratory polishing) [58,59].

A direct consequence of post-processing the surface or machining for a depth of 150 μm is that contouring strategy becomes ineffective
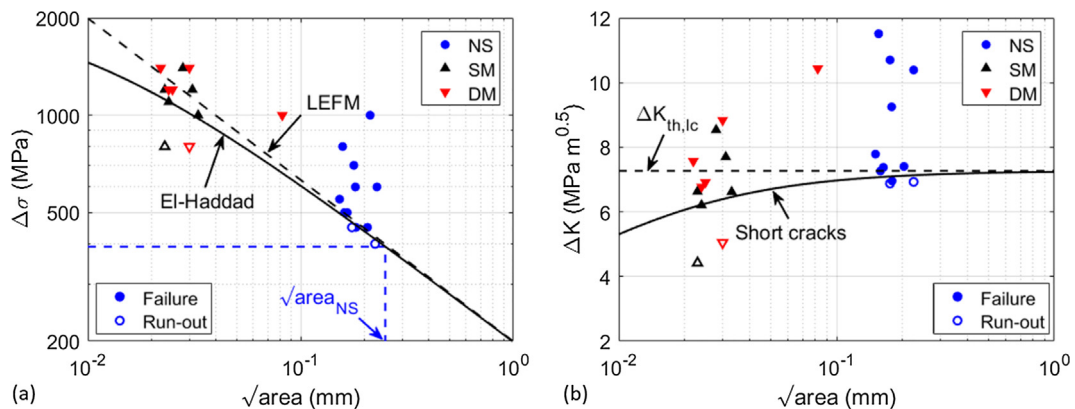

Fig. 12. Kitagawa diagram in terms of (a) stress, and (b) SIF range.
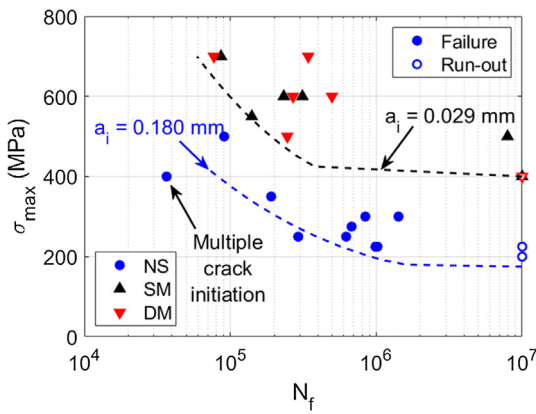
Fig. 13. Comparison of experimental stress-life fatigue data and the conservative fatigue curve predicted based on the most severe defect expected in the material. FCG simulations were performed using NASGRO.

Fig. 15. LEVD of experimental surface feature size for NS condition compared to the conservative estimate obtained via Eq. (5).

and loses its meaning, i.e. reducing surface roughness for NS parts. In this regard, using layer parameters optimized for reducing defects as those adopted in the rest of the specimen is expected to reduce the risk of creating large volumetric defects beneath the surface as those depicted in Fig. 1. Moreover, removing the contouring step during specimen fabrication would also guarantee more homogeneous cooling rates during the LB-PBF process, which could avoid introducing a sudden change in the grain size and orientation at the boundary between the two melting strategies [5].

Adopting Eq. (5), the assumption of considering the depth of a 2D shallow crack in the NS condition equal to the width of the contour layer (i.e. 80 μm) yields a critical defect size of 250 μm.

The size of the critical defects measured on the fracture surfaces of the NS specimens were interpolated described using a largest extreme value distribution (LEVD), as it is usually done for defects at the fracture origin [41,60], which is depicted in Fig. 15. The simple assumption based on the contour width proposed provides a conservative estimate of the maximum defect size for the NS condition, which can be used for preliminary fatigue strength assessment in the Kitagawa diagram or fatigue life assessment by FCG simulations and allows obtaining a conservative design curve. It is also worth remarking that the prospective distribution of fatigue life and strength can be estimated via theoretical Weibull-based models [61,62] or via computational models [63–65].

5. Conclusions

The fatigue and FCG properties of LB-PBF 17-4 PH SS subjected to CA-H1025 heat treatment procedure were investigated. Net-shape (NS) as well as shallow and deep machined (SM and DM) fatigue specimens
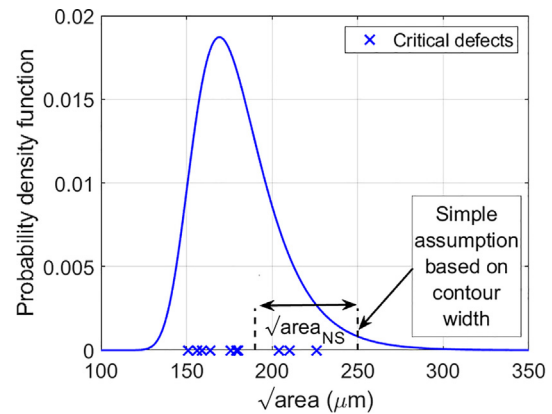
were considered to study the effect of surface machining including the depth of machining on the fatigue behavior of the material. The material was characterized for porosity size and distribution non-destructively via X-ray micro-CT, as well as destructively via analysis of polished sections, and fractography. Based on the results obtained, the following conclusions are drawn:

1. Shallow surface cracks due to the surface roughness were found to be responsible for the low fatigue resistance of net-shape LB-PBF 17-4 PH SS specimens. In contrast, cracks were initiated from sub-surface pores with the size of 20–30 μm in the machined specimens.
2. Significant improvement of HCF properties was obtained after machining (200–300 MPa increase in the fatigue strength). However, no evident improvements in fatigue performance were seen by increasing the machining allowance from 0.5 mm to 3 mm owing to the layer of surface flaws/asperities.
3. The Kitagawa diagram described in terms of $\sqrt{area}$ parameter evaluated the effect of both surface flaws and volumetric defects on fatigue strength, which showed an appropriate agreement with FCG tests results.
4. Although the typical pore size was characterized to be relatively small in machined specimens (around 20 μm, i.e., much smaller than the ones in net-shape specimens), these pores had a detrimental effect on the fatigue properties of the material. This is attributed to the increased strength of the material after CA-H1025 heat treatment, which increased the sensitivity to the presence of defects.
5. Characterizing the critical pores/defects by means of analyzing polished sections and fractography was found to be more efficient than by state-of-the-art X-ray micro-CT.
6. Fatigue life assessment by FCG simulations yielded correct estimates for both net-shape and machined specimens. In addition, using a
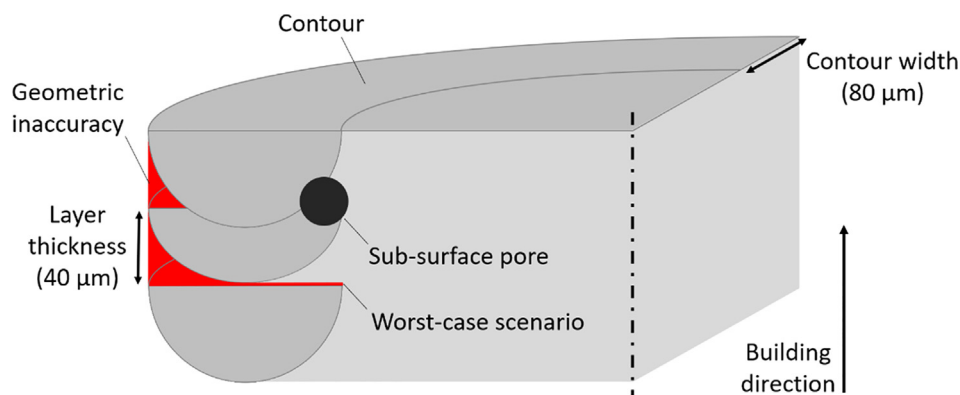

Fig. 14. Simplified schematic of geometric inaccuracy and sub-surface porosity created by contouring strategy.

simple evaluation, the detrimental effects of surface roughness on fatigue performance were proposed to be prevented by removing a surface depth of approximately 200 μm.

Declaration of competing interest

The authors declare that there is no conflict of interest.

Acknowledgements

Appendix A. Supplementary material

Supplementary data to this article can be found online at https://doi.org/10.1016/j.tafmec.2020.102477.

References

[1] A. Yadollahi, N. Shamsaei, Additive manufacturing of fatigue resistant materials: challenges and opportunities, Int. J. Fatigue. 98 (2017) 14–31, https://doi.org/10.1016/j.ijfatigue.2017.01.001.

[2] M. Seifi, A. Salem, J. Beuth, O. Harrysson, J.J. Lewandowski, Overview of materials qualification needs for metal additive manufacturing, Jom. 68 (2016) 747–764, https://doi.org/10.1007/s11837-015-1810-0.

[3] M. Seifi, M. Gorelik, J.M. Waller, N. Hrabe, N. Shamsaei, S.R. Daniewicz, J.J. Lewandowski, Progress towards metal additive manufacturing standardization to support qualification and certification, Jom 69 (2017) 439–455, https://doi.org/10.1007/s11837-017-2265-2.

[4] S. Romano, A.D. Brandão, J. Gumpinger, M. Gschweitl, S. Beretta, Qualification of AM parts: extreme value statistics applied to tomographic measurements, Mater. Des. 131 (2017) 32–48, https://doi.org/10.1016/j.matdes.2017.05.091.

[5] O. Andreau, E. Pessard, I. Koutiri, J.-D. Penot, C. Dupuy, N. Saintier, P. Peyre, A competition between the contour and hatching zones on the high cycle fatigue behaviour of a 316L stainless steel: analyzed using X-ray computed tomography, Mater. Sci. Eng. A. 757 (2019) 146–159, https://doi.org/10.1016/j.msea.2019.04.101.

[6] A. du Plessis, S.G. le Roux, G. Booysen, J. Els, Quality control of a laser additive manufactured medical implant by X-ray tomography, 3D print, Addit. Manuf. 3 (2016) 175–182, https://doi.org/10.1089/3dp.2016.0012.

[7] S. Beretta, S. Romano, A comparison of fatigue strength sensitivity to defects for materials manufactured by AM or traditional processes, Int. J. Fatigue. 94 (2017) 178–191, https://doi.org/10.1016/j.ijfatigue.2016.06.020.

[8] Y. Yamashita, T. Murakami, R. Mihara, M. Okada, Y. Murakami, Defect analysis and fatigue design basis for Ni-based superalloy 718 manufactured by selective laser melting, Int. J. Fatigue. 117 (2018) 485–495, https://doi.org/10.1016/j.ijfatigue.2018.08.002.

[9] J.N. Domfang Ngnekou, Y. Nadot, G. Henaff, J. Nicolai, W.H. Kan, J.M. Cairney, L. Ridosz, Fatigue properties of AlSi10Mg produced by additive layer manufacturing, Int. J. Fatigue. 119 (2019) 160–172, https://doi.org/10.1016/j.ijfatigue.2018.09.029.

[10] T. Persenot, A. Burr, G. Martin, J.-Y. Buffière, R. Dendievel, E. Maire, Effect of build orientation on the fatigue properties of as-built electron beam melted Ti-6Al-4V alloy, Int. J. Fatigue. 118 (2018) 65–76, https://doi.org/10.1016/j.ijfatigue.2018.08.006.

[11] S. Romano, A. Brückner-Foit, A.D. Brandão, J. Gumpinger, T. Ghidini, S. Beretta, Fatigue properties of AlSi10Mg obtained by additive manufacturing: defect-based modelling and prediction of fatigue strength, Eng. Fract. Mech. 187 (2018) 165–189, https://doi.org/10.1016/j.engfracmech.2017.11.002.

[12] S. Romano, L. Patriarca, S. Foletti, S. Beretta, LCF behaviour and a comprehensive life prediction model for AlSi10Mg obtained by SLM, Int. J. Fatigue. 117 (2018) 47–62, https://doi.org/10.1016/j.ijfatigue.2018.07.030.

[13] S. Romano, S. Miccoli, S. Beretta, A new FE post-processor for probabilistic fatigue assessment in the presence of defects and its application to AM parts, Int. J. Fatigue. 125 (2019) 324–341.

[14] H. Masuo, Y. Tanaka, S. Morokoshi, H. Yagura, T. Uchida, Y. Yamamoto, Y. Murakami, Influence of defects, surface roughness and HIP on the fatigue strength of Ti-6Al-4V manufactured by additive manufacturing, Int. J. Fatigue. 117

[15] M. Ciavarella, F. Monno, On the possible generalizations of the Kitagawa-Takahashi diagram and of the El Haddad equation to finite life, Int. J. Fatigue. 28 (2006) 1826–1837, https://doi.org/10.1016/j.ijfatigue.2005.12.001.

[16] B. Torries, A. Imandoust, S. Beretta, S. Shao, N. Shamsaei, Overview on microstructure- and defect-sensitive fatigue modeling of additively manufactured materials, Jom. 70 (2018) 1853–1862, https://doi.org/10.1007/s11837-018-2987-9.

[17] J. Gumpinger, A.D. Brandão, E. Beevers, T. Rohr, T. Ghidini, S. Beretta, S. Romano, Expression of additive manufacturing surface irregularities through a flaw-based assessment, ASTM Sel. Tech. Pap. 1620 (2019).

[18] M. Hamidi Nasab, D. Gastaldi, N.F. Lecis, M. Vedani, On morphological surface features of the parts printed by selective laser melting, (SLM), Addit. Manuf. 24 (2018) 373–377, https://doi.org/10.1016/j.addma.2018.10.011.

[19] J. Pegues, M.D. Roach, R.S. Williamson, N. Shamsaei, Surface roughness effects on the fatigue strength of additively manufactured Ti-6Al-4V, Int. J. Fatigue. 116 (2018) 543–552, https://doi.org/10.1016/j.ijfatigue.2018.07.013.

[20] F. Cabanettes, A. Joubert, G. Chardon, V. Dumas, J. Rech, C. Grosjean, Z. Dimkovski, Topography of as built surfaces generated in metal additive manufacturing: a multi scale analysis from form to roughness, Precis. Eng. 52 (2018) 249–265, https://doi.org/10.1016/j.precisioneng.2018.01.002.

[21] A. Triantaphyllou, C.L. Giusca, G.D. Macaulay, F. Roerig, M. Hoebel, R.K. Leach, B. Tomita, K.A. Milne, Surface texture measurement for additive manufacturing, Surf. Topogr. Metrol. Prop. 3 (2015) https://doi.org/10.1088/2051-672X/3/2/024002.

[22] Y. Tian, D. Tomus, P. Rometsch, X. Wu, Influences of processing parameters on surface roughness of Hastelloy X produced by selective laser melting, Addit. Manuf. (2017), https://doi.org/10.1016/j.addma.2016.10.010.

[23] J. Gockel, L. Sheridan, B. Koerper, B. Whip, The influence of additive manufacturing processing parameters on surface roughness and fatigue life, Int. J. Fatigue. 124 (2019) 380–388, https://doi.org/10.1016/J.IJFATIGUE.2019.03.025.

[24] J.W. Pegues, N. Shamsaei, M.D. Roach, R.S. Williamson, Fatigue life estimation of additive manufactured parts in the as-built surface condition, Mater. Des. Process. Commun. e36 (2019), https://doi.org/10.1002/mdp2.36.

[25] S. Romano, A. Abel, J. Gumpinger, A.D. Brandão, S. Beretta, Quality control of AlSi10Mg produced by SLM: metallography versus CT scans for critical defect size assessment, Addit. Manuf. 28 (2019) 394–405, https://doi.org/10.1016/j.addma.2019.05.017.

[26] E.W. Hovig, A.S. Azar, M.F. Sunding, K. Sørby, M.M'hamdi, E. Andreassen, High cycle fatigue life estimation of AlSi10Mg processed by laser powder bed fusion, MATEC Web Conf. 03015 (2018). doi: 10.1051/matecconf/201818803015.

[27] C.A. Kantzos, R.W. Cunningham, V. Tari, A.D. Rollett, Characterization of metal additive manufacturing surfaces using synchrotron X-ray CT and micromechanical modeling, Comput. Mech. 61 (2017) 575–580, https://doi.org/10.1007/s00466-017-1531-z.

[28] B. Vayssette, N. Saintier, C. Brugger, M. Elmay, E. Pessard, Surface roughness of Ti-6Al-4V parts obtained by SLM and EBM: effect on the high cycle fatigue life, Procedia Eng. 213 (2018) 89–97, https://doi.org/10.1016/j.proeng.2018.02.010.

[29] D. Greitemeier, C. Dalle Donne, F. Syassen, J. Eufinger, T. Melz, Effect of surface roughness on fatigue performance of additive manufactured Ti-6Al-4V, Mater. Sci. Technol. 32 (2015) 629–634, https://doi.org/10.1179/1743284715Y.0000000053.

[30] M. Gorelik, Additive manufacturing in the context of structural integrity, Int. J. Fatigue. 94 (2017) 168–177, https://doi.org/10.1016/j.ijfatigue.2016.07.005.

[31] G. Qian, Y. Hong, C. Zhou, Investigation of high cycle and Very-High-Cycle Fatigue behaviors for a structural steel with smooth and notched specimens, Eng. Fail. Anal. 17 (2010) 1517–1525, https://doi.org/10.1016/j.engfailanal.2010.06.002.

[32] R. Shrestha, J. Simsiriwong, N. Shamsaei, Fatigue behavior of additive manufactured 316L stainless steel parts: effects of layer orientation and surface roughness, Addit. Manuf. 28 (2019) 23–38, https://doi.org/10.1016/j.addma.2019.04.011.

[33] M.H. Nasab, S. Romano, D. Gastaldi, S. Beretta, M. Vedani, Combined effect of surface anomalies and volumetric defects on fatigue assessment of AlSi7Mg fabricated via laser powder bed fusion, Addit. Manuf. (2019), https://doi.org/10.1016/j.addma.2019.100918.

[34] P.D. Nezhadfar, R. Shrestha, N. Phan, N. Shamsaei, Fatigue behavior of additively manufactured 17-4 PH stainless steel: Synergistic effects of surface roughness and heat treatment, Int. J. Fatigue. 124 (2019) 188–204, https://doi.org/10.1016/j.ijfatigue.2019.02.039.

[35] A. Yadollahi, N. Shamsaei, S.M. Thompson, A. Elwany, L. Bian, Effects of building orientation and heat treatment on fatigue behavior of selective laser melted 17-4 PH stainless steel, Int. J. Fatigue. 94 (2017) 218–235, https://doi.org/10.1016/j.ijfatigue.2016.03.014.

[36] P.D. Nezhadfar, E. Burford, K. Anderson-wedge, B. Zhang, S.R. Daniewicz, N. Shamsaei, Fatigue crack growth behavior of additively manufactured 17-4 PH stainless steel: effects of build orientation and microstructure, Int. J. Fatigue. (2019), https://doi.org/10.1016/j.ijfatigue.2019.02.015.

[37] P.D. Nezhadfar, M. Masoomi, S.M. Thompson, N. Phan, N. Shamsaei, Mechanical properties of 17-4 PH stainless steel additively manufactured under Ar and N2 shielding gas, solid free. Fabr. Symp. (2017) 2430–2446.

[38] ISO 4288:1996 Geometrical Product Specifications (GPS), Surface texture: Profile method-Rules and procedures for the assessment of surface texture (ISO 4288: 1996), in: Ger. Version EN ISO, 1997. doi:1 0.1186/s40557-016-0111-6.

[39] ASTM E466 - 15, Standard Practice for conducting force controlled constant amplitude axial fatigue tests of metallic materials, (2015) 1–6. doi: 10.1520/E0466-15.2.

[40] BS ISO 12108:2018, BSI Standards Publication Metallic materials — Fatigue testing — Fatigue crack growth method, (2018).

[41] Y. Murakami, Metal Fatigue: Effects of Small Defects and Nonmetallic Inclusions, Elsevier, 2002.

[42] R. Shrestha, N. Shamsaei, M. Seifi, N. Phan, An investigation into specimen property to part performance relationships for laser beam powder bed fusion additive manufacturing, Addit. Manuf. 29 (2019), https://doi.org/10.1016/J.ADDMA.2019.100807.

[43] J.N. Domfang Ngnekou, J. Noel, N. Julien, N. Yves, H. Gilbert, R. Lionel, Influence of as-built surface and heat treatment on the fatigue resistance of Additively Layer Manufacturing (ALM) AlSi10Mg alloy, in: Fatigue 2018, Poitiers, France, 2018. doi:10.1051/matecconf/201816502004.

[44] South West Research Institute, NASGRO Reference Manual Version 8.2, 2017.

[45] J.C.J. Newman, A crack opening stress equation for fatigue crack growth, Int. J. Fract. 24 (1984) 131–135.

[46] H. Kitagawa, S. Takahashi, Applicability of fracture mechanics to very small cracks or cracks in the early stage, in: Proceeding Second Int. Conf. Mech. Behav. Mater., 1976: pp. 627–631.

[47] W.J. Dixon, A.M. Mood, A method for obtaining and analyzing sensitivity data, J. Am. Stat. Assoc. 43 (1948) 109–126. http://www.jstor.org/stable/2280071.

[48] ASTM E739, Standard Practice for Statistical Analysis of Linear or Linearized Stress-Life (S-N) and Strain-Life (ε-N) Fatigue Data, Annu. B. ASTM Stand. (2015) 1–7. doi:10.1520/E0739-10.2.

[49] DNVGL-RP-C210, Probabilistic methods for planning of inspection for fatigue cracks in offshore structures, 2015.

[50] S. Siddique, M. Imran, M. Rauer, M. Kaloudis, E. Wycisk, C. Emmelmann, F. Walther, Computed tomography for characterization of fatigue performance of selective laser melted parts, Mater. Des. 83 (2015) 661–669, https://doi.org/10.1016/j.matdes.2015.06.063.

[51] L. Carneiro, B. Jalalahmadi, A. Ashtekar, Y. Jiang, Cyclic deformation and fatigue behavior of additively manufactured 17-4 PH stainless steel, Int. J. Fatigue 123 (2019) 22–30, https://doi.org/10.1016/j.ijfatigue.2019.02.006.

[52] K. Takahashi, Y. Murakami, Quantitative evaluation of effect of surface roughness on fatigue strength. In: J.H.B. and M.W.B. and R.A.S. and T.C.L. and B. Tomkins (Ed.), Eng. Against Fatigue, Balkema Publishers, 1999: pp. 693–703.

[53] J. Zhang, A. Fatemi, Surface roughness effect on multiaxial fatigue behavior of additive manufactured metals and its modeling, Theor. Appl. Fract. Mech. 103 (2019) 102260, https://doi.org/10.1016/j.tafmec.2019.102260.

[54] A. Yadollahi, M.J. Mahtabi, A. Khalili, H.R. Doude, J.C.J. Newman, Fatigue life prediction of additively manufactured material: effects of surface roughness, defect size, and shape, Fatigue Fract. Eng. Mater. Struct. (2018) 1–13, https://doi.org/10.1111/ffe.12799.

[55] M.H. El Haddad, T.H. Topper, K.N. Smith, Prediction of non propagating cracks, Eng. Fract. Mech. 11 (1979) 573–584, https://doi.org/10.1016/0013-7944(79)90081-X.

[56] K.J. Miller, The short crack problem, Fatigue Fract. Eng. Mater. Struct. 5 (1982) 223–232.

[57] V.-D. Le, E. Pessard, F. Morel, F. Edy, Interpretation of the fatigue anisotropy of additively manufactured TA6V alloys via a fracture mechanics approach, Eng. Fract. Mech. (2019), https://doi.org/10.1016/j.engfracmech.2019.03.048.

[58] E. Beevers, A.D. Brandão, J. Gumpinger, M. Gschweitl, C. Seyfert, P. Hofbauer, T. Rohr, T. Ghidini, Fatigue properties and material characteristics of additively manufactured AlSi10Mg – effect of the contour parameter on the microstructure, density, residual stress, roughness and mechanical properties, Int. J. Fatigue. 117 (2018) 148–162, https://doi.org/10.1016/j.ijfatigue.2018.08.023.

[59] B. AlMangour, J.M. Yang, Improving the surface quality and mechanical properties by shot-peening of 17-4 stainless steel fabricated by additive manufacturing, Mater. Des. 110 (2016) 914–924, https://doi.org/10.1016/j.matdes.2016.08.037.

[60] S. Beretta, Y. Murakami, Statistical analysis of defects for fatigue strength prediction and quality control of materials, Fatigue Fract. Eng. Mater. Struct. 21 (1998) 1049–1065, https://doi.org/10.1046/j.1460-2695.1998.00104.x.

[61] A. Wormsen, B. Sjödin, G. Härkegård, A. Fjeldstad, Non-local stress approach for fatigue assessment based on weakest-link theory and statistics of extremes, Fatigue Fract. Eng. Mater. Struct. 30 (2007) 1214–1227, https://doi.org/10.1111/j.1460-2695.2007.01190.x.

[62] G. Qian, W.-S. Lei, A statistical model of fatigue failure incorporating effects of specimen size and load amplitude on fatigue life, 6435 (2019). doi: 10.1080/14786435.2019.1609707.

[63] A. Wormsen, A. Fjeldstad, G. Härkegård, A post-processor for fatigue crack growth analysis based on a finite element stress field, Comput. Methods Appl. Mech. Eng. 197 (2008) 834–845, https://doi.org/10.1016/j.cma.2007.09.012.

[64] R.C. McClung, Y. Lee, M.P. Enright, New Methods for Automated Fatigue Crack Growth and Reliability Analysis, 136 (2014). doi: 10.1115/1.4026140.

[65] S. Romano, S. Beretta, S. Miccoli, M. Gschweitl, Probabilistic framework for defect tolerant fatigue assessment of AM parts applied to a space component, ASTM Sel. Tech. Pap. 1620 (2019).